The electrochemical behaviour of Ti-48Al-2Cr-2Nb produced by electron beam powder bed fusion process

Intermetallics 175 (2024) 108472

Contents lists available at ScienceDirect

Intermetallics

journal homepage: www.elsevier.com/locate/intermet

The electrochemical behaviour of Ti-48Al-2Cr-2Nb produced by electron beam powder bed fusion process

Amir behjat, Abdollah Saboori *, Manuela Galati, Luca Iuliano

Integrated Additive Manufacturing Center, Department Management and Production Engineering, Politecnico di Torino, Corso Duca Degli Abruzzi 24, 10129, Torino, Italy

ARTICLE INFO

Keywords:
Additive manufacturing
Electron beam powder bed fusion
Titanium aluminides
Corrosion behaviour
Passive film
Vacancies

ABSTRACT

Titanium aluminides (TiAl) are distinguished by their exceptional strength-to-weight ratio, making them ideal for aerospace and medical applications. Notably, TiAl alloys offer a unique combination of high-temperature resistance and corrosion resilience, contributing to their growing prominence in advanced engineering and biomedical fields. Although initially developed for aerospace applications, TiAl alloys have demonstrated promising potential as implant materials over time. Hence, this research focuses on producing γ-TiAl alloy through electron beam powder bed fusion (EB-PBF) technology, utilising a powder with a composition of Ti-48Al-2Cr-2Nb. For comparative purposes, the corrosion characteristics of Ti6Al4V produced via EB-PBF were also evaluated under identical conditions. The findings indicate that the EB-PBF γ-TiAl exhibits exceptional resistance to corrosion. This is supported by the significantly high polarisation resistance and corrosion potential values, as well as the notably low corrosion current value. However, based on the analysis of the polarisation and impedance curves, it can be observed that the γ-TiAl sample displayed a less protective passive film formation. This occurrence can be attributed to the presence of aluminium ions within the passive layer, resulting in the formation of unstable oxides. As a consequence, it can be inferred that γ-TiAl exhibits inferior resistance to pitting corrosion when compared to Ti6Al4V alloy. The point defect model and Mott-Schottky test further revealed that the γ-TiAl alloy exhibited increased oxygen vacancies. Additionally, the presence of aluminium ions as impurities or dopants led to their substitution for titanium ions, creating cationic vacancies within the passive film. The accumulation of excessive cation vacancies ultimately led to the initiation of pitting corrosion.

1. Introduction

Nowadays, there is a substantial and continually rising need for resilient implants, especially in the context of dental and orthopaedic replacements [1,2]. Titanium and its alloys have emerged as preferred choices for implant materials owing to their exceptional biocompatibility and superior mechanical strength. However, it is well documented that the success of implantation does not solely depend on the mechanical properties of the material, but its functional characteristics, such as corrosion behaviour in bodily fluids, also play a crucial role [3,4].

Generally, Ti-based biomaterials exhibit relatively high corrosion resistance under normal physiological conditions, primarily attributed to the presence of a passive oxide layer. This oxide layer, typically in the range of 4–6 nm, spontaneously forms at room temperature and serves as a protective barrier on the surface of the components [5,6].

Ti6Al4V is the most common titanium alloy used in bone repair and replacement [7,8]. However, its applications as a biomaterial are faced with some limitations. For instance, one notable concern is the potential release of vanadium ions, which are considered toxic and can cause allergic and inflammatory reactions [9]. Additionally, the low wear resistance of Ti6Al4V is another significant issue that needs to be addressed when considering its suitability as a biomaterial [10,11].

Recently, there has been growing interest in exploring titanium aluminide (TiAl) intermetallics as potential alternatives to replace Ti6Al4V, which are primarily developed for aerospace and automotive applications [12,13]. γ-TiAl alloys exhibit several unique properties, including low density, high strength-to-weight ratio, and excellent stiffness and strength. These attributes make them appealing candidates for various applications, particularly in the field of biomaterials [14].

Apart from the advancement of new titanium alloys, significant efforts are being directed towards the production of intricate components

* Corresponding author.
E-mail address: abdollah.saboori@polito.it (A. Saboori).

https://doi.org/10.1016/j.intermet.2024.108472
Received 18 June 2024; Received in revised form 21 August 2024; Accepted 31 August 2024
Available online 5 September 2024

in a controlled vacuum environment, free from oxidation or contamination, using innovative techniques. One such promising approach is additive manufacturing, which offers immense potential in fabricating complex parts directly from powdered materials. This technique enables precise control over the manufacturing process, allowing for the creation of intricate and customised designs with enhanced efficiency and accuracy [15–18].

The electron beam powder bed fusion (EB-PBF) process is an additive manufacturing technique that uses a high-energy electron beam to construct complex parts from a powder bed layer-by-layer [19]. This process enables the creation of near-net shape components with intricate geometries. While significant research has been conducted on the EB-PBF of γ-TiAl alloy in recent years [13,20–25], limited information is available concerning its electrochemical performance. It should be highlighted that existing literature primarily focuses on the corrosion properties of EB-PBF γ-TiAl alloy in the context of high-temperature oxidation resistance [26,27], with less emphasis on its behaviour in corrosive environments at normal physiological conditions [28,29].

Currently, there is insufficient information about the corrosion mechanisms of γ-TiAl alloys fabricated through the EB-PBF process for biomedical purposes. Therefore, this study seeks to explore the electrochemical dissolution behaviour of EB-PBFed γ-TiAl alloys in a 0.9 % NaCl solution. Through this investigation, we aim to gain a more comprehensive understanding of the electrochemical characteristics of γ-TiAl alloys produced via EB-PBF, which will, in turn, contribute to advancing the development of enhanced corrosion-resistant materials for biomedical applications.

2. Material and methods

Parallelepiped samples ($18 \times 18 \times 15$ mm^3) were produced using an Arcam A2X, an EB-PBF machine, operating at a constant acceleration voltage of 60 kV. The selected material for the study was γ-TiAl alloy powder purchased from Arcam with a composition of Ti-48Al-2Cr-2Nb, with a particle size in the range of 55–150 μm and an average size of 75 μm. The samples were printed with a layer thickness of 90 μm. The preheating temperature of the powder bed was set to 1050 °C, according to Ref. [20]. A hatching mode was used to selectively melt the powder layer according to the 2D Section. In addition, at each layer, the scanning path was rotated by 90°. The process parameters for the melting were 9 mA for the beam current, sped equal to 1350 mm/s and 0.3 mm of line offset. For comparison purposes, Ti6Al4V samples of the same size were produced, tested and served as a reference. The Ti6Al4V samples were printed using standard parameters, as reported in Ref. [30]. The chemical compositions of the precursor powders are shown in Table 1.

The microstructural analysis of the samples was carried out using both optical microscopy (OM, Nikon EpipHot 300) and scanning electron microscopy (SEM, Philips XL 30) in conjunction with energy dispersive spectroscopy (EDS). Prior to analysis, the samples were prepared by grinding and polishing to 1 μm with alumina suspension and subsequent etching in Kroll's reagent. X-ray diffraction (XRD) analysis was performed on the cross-sectional plane (x-z plane, along the build direction) of the samples to investigate the phase composition of the as-built samples. This analysis was carried out using a Philips X-ray diffractometer equipped with a Mo Kα X-ray target (0.7093 Å). The working voltage and current were set to 40 kV and 30 mA, respectively. The samples were scanned in a 2θ range of 15°–40° with a step size of 0.02° to determine the phase composition of the alloys.

Table 1
Chemical composition of the as-received Ti6Al4V and γ-TiAl alloy powders in at % and wt% units.

	Element	Al	V	Cr	Nb	Ti
Ti6Al4V	wt.%	6	4	–	–	Bal.
	at.%	10.6	1.9	–	–	Bal.
γ-TiAl	wt.%	33.4	–	2.4	4.8	Bal.
	at.%	48	–	2	2	Bal.

The electrochemical tests were carried out using a three-electrode system and an electrochemical workstation (PARSTAT 2273, Princeton Applied Research, USA). In this setup, a platinum sheet served as the counter electrode, an Ag/AgCl electrode was used as the reference electrode, and the samples served as the working electrode. Before the tests, the surface of the samples were mechanically polished using silicon carbide abrasive papers up to a grit size of #2000 and then degreased in acetone. They were then rinsed with distilled water and dried in the air. The electrolyte solution utilised for the experiments was a 0.9 wt% NaCl solution, which was kept at room temperature. In the first step, the open circuit potential (OCP) was monitored for 60 min. Subsequently, electrochemical impedance spectroscopy (EIS) was performed, measuring the impedance over a frequency range of 10^{-2} to 10^{5} Hz and an AC amplitude of 10 mV. In the next step, the Mott-Schottky (MS) relationship was measured at a frequency of 1 kHz. In the MS measurements, the potential was swept from an initial potential of 0.6 $V_{Ag/AgCl}$ to a final potential of −1.2 $V_{Ag/AgCl}$ in the cathodic direction. The step size for each potential increase was set to 10 mV/s. Subsequently, potentiodynamic polarisation measurements (PDP) were conducted with a scanning rate of 1 mV/s. The potential range for the PDP measurements ranged from −250 to 1200 $mV_{Ag/AgCl}$ relative to the OCP. Electrochemical experiments were performed three times to ensure the reproducibility of the data.

After the PDP test, the morphology of the sample surfaces was examined after corrosion. This analysis was performed using SEM in combination with EDS. SEM allows the observation of surface features and morphological changes, while EDS provides information on the elemental composition of the corroded regions.

Inductively coupled plasma mass spectrometry (ICP-MS) was employed to quantify the release of Ti and Al ions from the Ti6Al4V and γ-TiAl alloys produced via EB-PBF into the electrolyte after anodic polarisation.

3. Results and discussion

Fig. 1(a and b) shows the typical XRD profiles of the as-built samples. Based on previous works [31,32], most of the peaks in the Ti6Al4V sample corresponded to the α (or α′) phase and a small portion to the β phase. For the γ-TiAl sample, the XRD pattern displayed the crystal structures of the hexagonal close-packed (HCP) α_2-Ti_3Al phase and the face-centered tetragonal γ-TiAl phase. As shown in Fig. 1 (b), the strongest diffraction peak was at 17.66°, which belonged to (111) γ, and thus γ was identified as the matrix phase. These findings are consistent with the known crystal structures of the γ-TiAl and α-Ti_3Al phases in the γ-TiAl alloy [20,33].

Typical microstructures of the EB-PBF processed Ti6Al4V and γ-TiAl are shown in Fig. 1(c–f). Based on the outcomes of the microstructural analysis presented in Fig. 1(c–e), the microstructure of the as-built Ti6Al4V exhibited a relatively fine α lamellar structure, which is due to the nature of the EB-PBF process as a rapid solidification process. For the γ-TiAl sample, lamellar colonies composed of dual phases with gamma grains can be seen in Fig. 1(d–f). These lamellar colonies, namely (α_2+γ)-TiAl, consist mainly of alternating γ and α_2 phases. Dark grey regions represent the α_2 phase, while the γ phase are depicted as light grey regions. According to the Ti-Al phase diagram [34], various microstructures can be formed depending on the Al content. In addition, microstructural evolution can be significantly affected by varying the heat input, the important factor being the cooling rate. The formation mechanism of the microstructure along the building direction has been investigated in previous studies [20,35].

The chemical composition and microstructure of metals play a significant role in determining their corrosion behaviour in various environments, including medical solutions [5,10]. In an attempt to provide

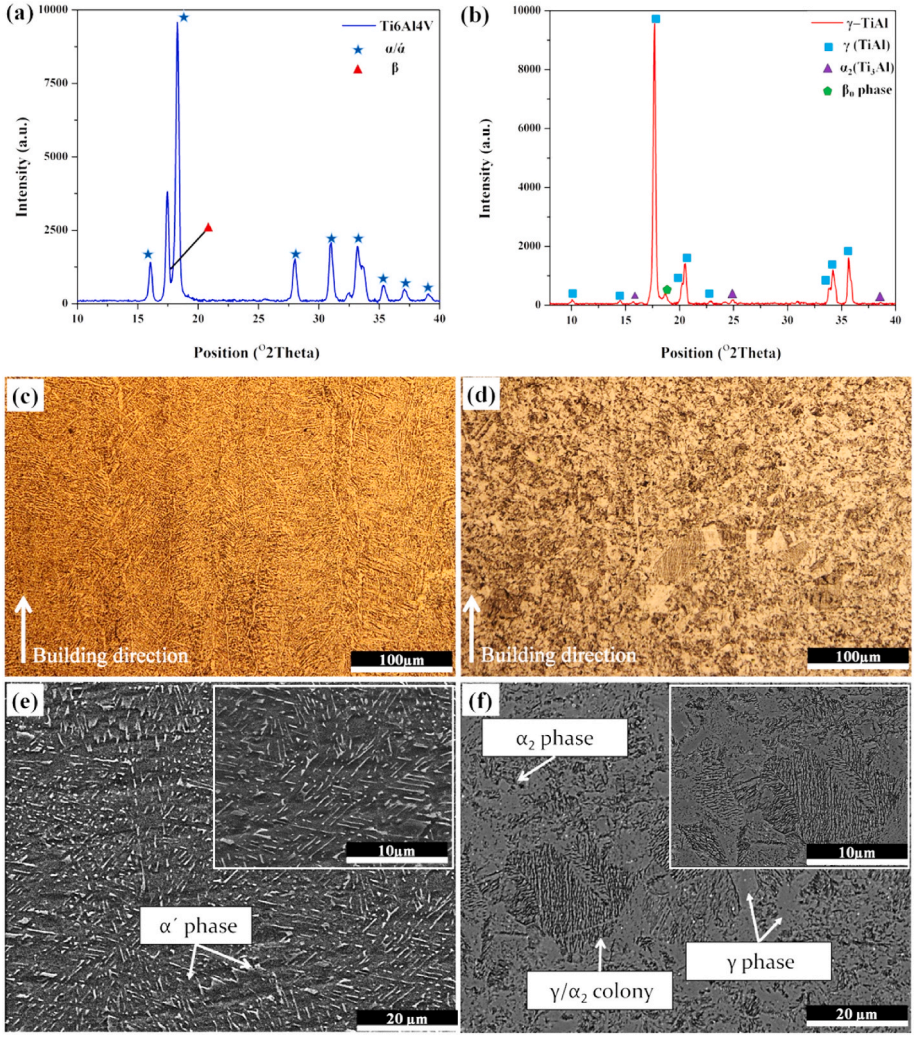

Fig. 1. Microstructural features of EB-PBF-produced samples: (a,b) XRD pattern, OM and SEM of (c,e) Ti6Al4V and (d,f) γ-TiAl alloy.

insights into understanding the corrosion behaviour and electronic properties of the passive films of Ti6Al4V and γ-TiAl, potentiodynamic polarisation, electrochemical impedance spectroscopy and Mott-Schottky measurements were performed in 0.9 wt% NaCl solution at room temperature.

Fig. 2(a) shows the results of the OCP examination performed on the Ti6Al4V and γ-TiAl alloys. The curves demonstrate a gradual increase towards a more positive potential until both alloys reach an almost constant value. These outcomes indicate the spontaneous formation of an oxide film on the surfaces of the samples during the test duration of

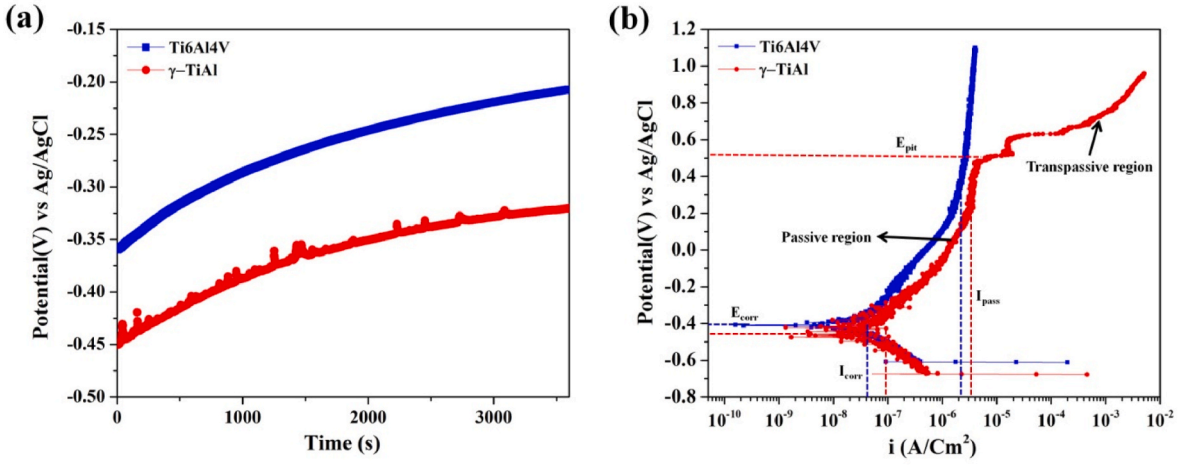

Fig. 2. (a) Open circuit potential measurements, (b) potentiodynamic polarisation curves of EB-PBF-produced Ti6Al4V and γ-TiAl alloy for 1 h in 0.9 % NaCl solution.

3600 s. This oxide film acts as a protective layer that passivates the metallic surface upon contact with the electrolyte [36,37].

Fig. 2(b) displays the potentiodynamic polarisation curves of Ti6Al4V and γ-TiAl alloys. From these curves, various electrochemical parameters were determined to assess the corrosion behaviour of the alloys. The values of the corrosion potential (E_{corr}), the corrosion current density (I_{corr}), the passive current density (I_{pass}), and the breakdown potential (E_b) are listed in Table 2. The passive current densities were determined specifically at a point in the middle of the passive region.

Based on the potentiodynamic curves and the electrochemical parameter data, it can be concluded that both the Ti6Al4V and the γ-TiAl alloys exhibit typical passive behaviour in the anodic branches of the polarisation curves, which is characterised by low current densities. The E_{corr} and I_{corr} values of the γ-TiAl intermetallic alloy did not differ significantly from those of the Ti6Al4V alloy sample (Table 2).

According to Faradays law [38], the corrosion rate is directly related to I_{corr}, with a higher I_{corr} indicating a higher corrosion rate of the samples. Therefore, the slightly higher I_{corr} for the γ-TiAl alloy indicates a relatively higher corrosion rate and fast dissolution kinetics compared to the Ti6Al4V alloy. In addition, a slight shift in corrosion potential towards more cathodic values (lower E_{corr}) was observed for the γ-TiAl alloy, which can be attributed to the addition of aluminium. This shift indicates a less noble character of the aluminium in the alloy, which may contribute to its corrosion behaviour [39]. Furthermore, when the samples are in the passive region, the current remains relatively constant and exhibits only minimal fluctuations. This behaviour suggests the spontaneous formation of a passive film above the corrosion potential, resulting from chemical reactions that impede further metal dissolution. However, it is evident that the protective ability of the oxide layer on the γ-TiAl alloy is inferior to that of Ti6Al4V, as indicated by the observed increase in passive current density (I_{pass}).

The most noticeable difference observed in the passive regions of the two alloys is the lack of a passivity breakdown in Ti6Al4V, while a well-defined breakdown potential is clearly evident in the γ-TiAl alloy, characterised by a sharp increase in anodic current densities at 0.53 ± (0.11) $V_{Ag/AgCl}$. This indicates that γ-TiAl has a weaker resistance to pitting corrosion compared to the Ti6Al4V alloy as the passive film breaks down and the pits start to grow. Pitting corrosion is widely recognised as one of the most detrimental and insidious types of corrosion. Moreover, the breakdown potential indicates the localised breakdown of the passive film and can be utilised as a measure of resistance to localised corrosion. Actually, when the breakdown potential is exceeded, the passive film ruptures, leading to a rapid increase in current density [38]. One possible explanation for this phenomenon is the increased electrochemical activity resulting from the higher aluminium content in the γ-TiAl matrix compared to Ti6Al4V. This higher aluminium content leads to a significantly lower standard electrode potential compared to titanium, thus contributing to the observed differences in breakdown behaviour [40].

Studies have reported that the composition of the surface passive film of Ti6Al4V consists primarily of a compact oxidation film of TiO_2, whereas the passive film in γ-TiAl is composed of TiO_2 and Al_2O_3 [40,41]. As a result, the Ti6Al4V alloy exhibits a wide passivation window with no sign of breakdown or pitting, even at high potentials. This superior resistance to the formation and growth of stable corrosion pits indicates the presence of a more stable passive film in the chloride-containing electrolyte for Ti6Al4V.

The EIS test was used to assess the condition of the alloy surfaces after being exposed to solutions for 1 h. Fig. 3 (a, b) illustrates the Nyquist and Bode diagrams, representing the passive film characteristics of the γ-TiAl and Ti6Al4V alloys.

In the Nyquist plot, a clear semicircle shape can be seen, which is primarily associated with the charge transfer process at the interface between the solution and the anode. The diameter of this semicircle is linked to the polarisation resistance of the electrode in the solution and reflects its corrosion resistance. Consequently, the Ti6Al4V alloy has a higher polarisation resistance compared to the γ-TiAl alloy. As for the Bode plot diagram shown in Fig. 3(b), the high impedance values and phase angle indicate the presence of a single thin passive oxide layer on the surface of both samples [38].

The results of the bode phase diagram indicate that the impedance increases as the scanning frequency decreases and reaches its maximum value at 10 mHz, which is due to the high polarisation resistance of the samples. However, when comparing the two alloys, the Ti6Al4V alloy exhibits an even stronger capacitive behaviour with a phase angle approaching 80° over a wide frequency range. This finding supports the presence of an impermeable and passive layer formed on the Ti6Al4V alloy, as well as the high values of polarisation resistance (R_p) that emerge from the Nyquist plot. In addition, changes in the resistance of the passive film in the materials can be attributed to structural changes in the film itself or to changes in the ionic or electrical conductivity of the film. These factors can influence the overall impedance behaviour observed during the EIS test.

To obtain a more quantitative analysis of the experimental EIS data for both samples, an equivalent electrical circuit (EEC) was used. The EEC shown in Fig. 3 is commonly utilised for passive metals [42]. In this circuit, R_s stands for the solution resistance, R_p denotes the polarisation resistance, and CPE represents the constant phase element. The CPE is used to describe the non-ideal behaviour of a capacitor and its impedance can be expressed as follows [42]:

$$Z_{CPE} = \frac{1}{Q(\omega j)^{n}} \quad (1)$$

where the *CPE* constant is represented by *Q*, the angular frequency by ω (in radians per second), the imaginary number by *j*, and the *CPE* exponent by *n*. It is important to highlight that the CPE exponent (n) is associated with different parameters, where a value of 1 is assumed for an ideal capacitor and values between 0 and 1 are assumed for non-ideal capacitive behaviour [42]. The fitted parameter values can be found in Table 3.

According to the data presented in Table 3, both alloys exhibit high corrosion resistance, which is indicated by the high R_p value and the low CPE value. The CPE value in the equivalent electrical circuit is positively correlated with the ion diffusivity within the passive film. Therefore, the significantly lower CPE value observed for Ti6Al4V indicates a higher compactness of the passive film formed on this alloy compared to γ-TiAl. This indicates that the passive film on Ti6Al4V is denser and provides stronger protection against corrosion.

The thickness of the passive film can also be estimated using equation (2) as follows [43]:

$$Lss = \frac{\varepsilon\varepsilon_0}{C_{eff}} \quad (2)$$

Here, ε_0 stands for the vacuum permittivity (8.854×10^{-14} Fcm^{-1}), ε for the dielectric constant of the passive film (approximately 60 for the TiO_2 passive film [42]), *A* for the effective area of the electrode and C_{eff} for the effective capacitance. The value of C_{eff} can be calculated using equation (3) [44]:

$$C_{eff} = \sqrt[n]{Q.R_t^{1-n}} \quad (3)$$

where R_t is the sum of the total resistance (*Rs* and *Rp*). By utilising the values of *n* and *CPE* obtained from the experimental EIS data fitting, the passive film thicknesses were calculated and presented in Table 3.

Table 2
Summary of electrochemical parameters obtained for 1 h in 0.9 % NaCl solution.

Sample	I_{corr} (μA/cm^2)	I_{pass} (μA/cm^2)	E_{corr}($V_{Ag/AgCl}$)	E_{pit} ($V_{Ag/AgCl}$)
Ti6Al4V	0.034 ± 0.012	1.22 ± 0.03	−0.41 ± 0.23	–
γ-TiAl	0.092 ± 0.038	2.34 ± 0.05	−0.46 ± 0.11	0.53 ± 0.11

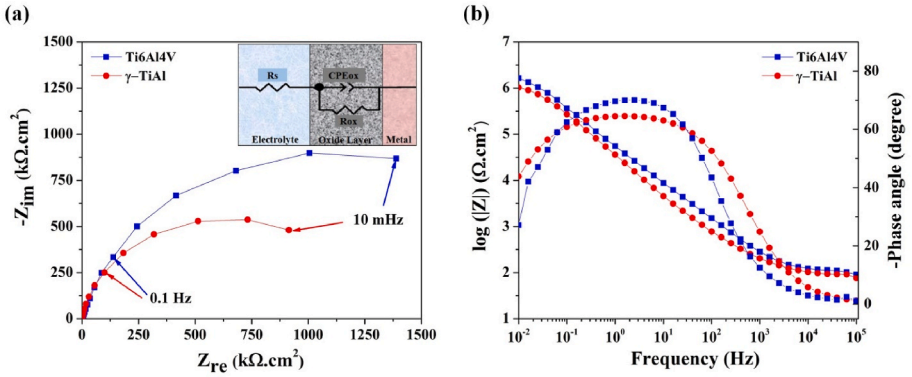

Fig. 3. EIS plots for the EB-PBF-produced Ti6Al4V and γ-TiAl alloy for 1 h in 0.9 % NaCl solution: (a) Nyquist plots and (b) Bode plots (Inset shows the equivalent circuit used to fit the data).

Table 3
Variations in the impedance parameters and passive film thickness of all samples for 1 h in 0.9 % NaCl solution.

Sample	Rs (Ω. cm^2)	Rp (MΩ. cm^2)	CPE ($\mu\Omega^{-1}\bullet s^n \bullet cm^{-2}$)	n	L (nm)
Ti6Al4V	106.2 ± 0.3	2.76 ± 0.37	3.79 ± 0.61	0.80 ± 0.06	2.8-3.1
γ-TiAl	105.9 ± 0.3	1.49 ± 0.72	5.68 ± 0.32	0.84 ± 0.07	3.9-4.6

From the results of the EIS test, it is evident that the presence of aluminium in the γ-TiAl alloys has an impact on the characteristics of the passive film compared to Ti6Al4V. The aluminium content leads to the formation of a thicker oxide layer; however, this oxide layer is more porous and less protective. Previous literature supports this observation and attributes it to the increased formation of aluminium oxides in the film [39,45]. These aluminium oxides contribute to the formation of porous oxide layers, resulting in a thicker passive layer. Additionally, the lower proportion of titanium oxides (TiO_2) in the film, which play a crucial role in maintaining passivity, has a negative effect on corrosion resistance. Consequently, the protection provided by the oxide layer in the γ-TiAl alloy is lower than that in Ti6Al4V. This is reflected in the increased values of I_{corr} and I_{pass} in Table 2, despite the thickening of the passive film.

The M − S tests could explain the semi-conductive behaviour of the formed passive film on passive metals. Fig. 4 shows the M − S curves for both samples in 0.9 % NaCl.

The M − S curves reveal linear regions with positive slopes in the range between −0.8 $V_{Ag/AgCl}$ and −0.3 $V_{Ag/AgCl}$. These positive slopes indicate n-type semiconductor behaviour. This observation suggests that the primary charge carriers in the passive films are oxygen vacancies, which act as anion donors [46]. The donor densities (ND) of the oxide films formed on both samples can be determined by calculating the slopes of the linear region in the M − S curves using equation (4):

$$N_D = \frac{2}{\varepsilon\varepsilon_0 e a} \quad (4)$$

where e is the elementary charge (1.6×10^{-19} C), and a is the slope in the n-type range. The estimated N_D values for Ti6Al4V and γ-TiAl alloys are 9.22 ± (0.77) × 10^{19} cm^{-3} and 19.83 ± (1.24) × 10^{19} cm^{-3}, respectively. The donor density in the oxide layer formed on titanium is typically lower (in the order of 10^{19}-10^{20} cm^{-3}) compared to that of most passive metals such as nickel (Ni) [47] and iron-steel (Fe) [43,46,48] (in the range of 10^{20}-10^{21} cm^{-3}). This difference in donor density could contribute to the exceptional resistance of titanium alloys to both uniform corrosion and pitting corrosion [49].

The obtained N_D values indicate that the passive film formed on TiAl has a higher N_D compared to Ti6Al4V. This suggests that the oxide film on γ-TiAl is less protective, which aligns with previous findings from polarisation and EIS measurements. Based on these results, it can be deduced that the oxide layer on the γ-TiAl alloy has a higher density of defects. Point defects, particularly oxygen vacancies in n-type semiconductors, play a crucial role in the stability of the passive film and the initiation of localised corrosion processes [49,50]. The n-type semiconducting behaviour of the passive film is closely associated with susceptibility to pitting corrosion. Furthermore, passive films with high donor density are known to favor chloride adsorption, which enhances pit nucleation and growth [38,51]. Consequently, the γ-TiAl alloy is more susceptible to pitting corrosion compared to the Ti6Al4V alloy (Fig. 2), indicating an interplay between the electronic structure of the passive film and its susceptibility to localised corrosion attack.

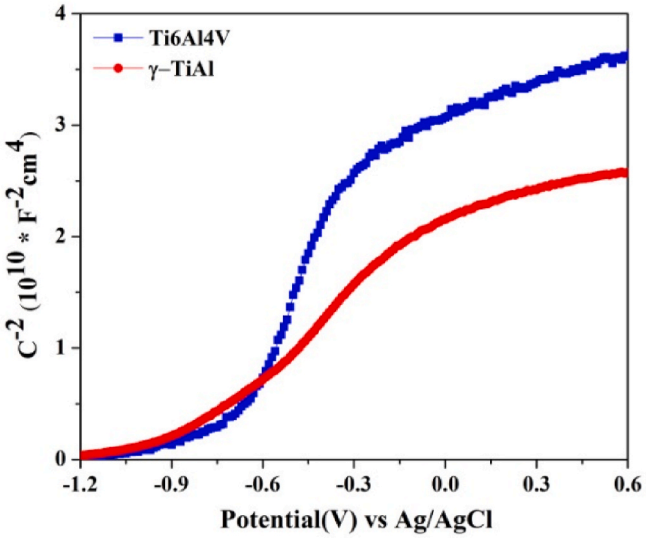

Fig. 4. Mott-Schottky curves at frequency 1 kHz measured in the cathodic direction for EB-PBF-produced Ti6Al4V and γ-TiAl alloy for 1 h in 0.9 % NaCl solution.

Fig. 5 shows the concentrations of Ti and Al ions released into the electrolytes by the tested samples. In an aqueous solution, the main source of released metal ions is the dissolution of the passive film. Interestingly, despite the significant difference in aluminium content, the Ti ion release from the γ-TiAl alloy is similar to that of the Ti6Al4V alloy. Previous studies have reported that Al^{3+} ions are usually associated with oxygen vacancies in the passive film [52]. When oxygen vacancies are trapped by halide ions such as Cl^- on the film surface, anion/cation vacancy pairs are formed, releasing metal ions [51]. Due to

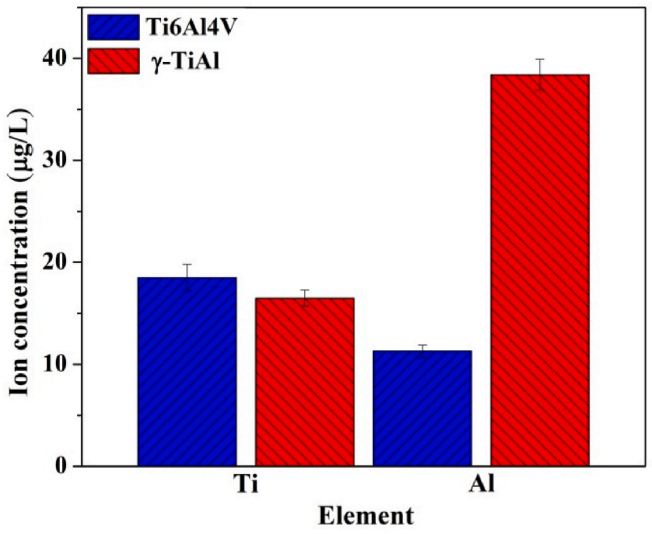

Fig. 5. Releasing of metal ions into the 0.9 % NaCl solution after anodic polarisation testing.

the higher aluminium content in the intermetallic γ-TiAl alloy (48 vs. 10.6 at.%), Al^{3+} ions are also more prone to be released into the solution from the γ-TiAl alloy than from Ti6Al4V.

Fig. 6 displays the surface morphology of the experimental samples before and after the polarisation test. Before the test, the surface appears clear and homogeneous (Fig. 6(a and b)). The EDS analysis reveals that the weight percentages of the elements present on the surface of both alloys are almost identical to those of the alloy matrix. However, after the polarisation test, the micrograph of γ-TiAl in NaCl shows the presence of several pits on the alloy surface, indicating the collapse of the oxide film (Fig. 6 (d)). In contrast, as shown in Fig. 6 (c), the Ti6Al4V sample exhibits only thin oxide films on the surface, which is consistent with the polarisation curve shown in Fig. 2. The EDS analysis in Fig. 6(c and d) indicates that the presence of oxygen contributes to the formation of ceramic phases such as TiO_2 and Al_2O_3. Furthermore, the EDS results for the γ-TiAl alloy indicate that the composition of the non-corroded regions remains relatively unchanged after the polarisation test. However, the corroded area shows a significant decrease in aluminium content. It is noteworthy that the passive film formed on the surface of Ti6Al4V has a lower defect density (as shown in Fig. 4), which effectively prevents further corrosion reactions.

Fig. 6(e–j) presents high-magnification SEM images and EDX map analysis conducted on the dissolution morphologies and pit analysis of the γ-TiAl alloy. The EDX map analysis reveals a decrease in the aluminium content compared to its original content before the test. This suggests that the corrosion of the alloy may have been caused by the dissolution of aluminum, leading to the formation of aluminium depletion zones around the pits under the attack of chloride ions. Additionally, the presence of oxygen is likely due to the formation of an Al_2O_3 layer on the surface of the alloy, which helps to reduce the corrosion of the γ-TiAl alloy. The atomic percentage and solute

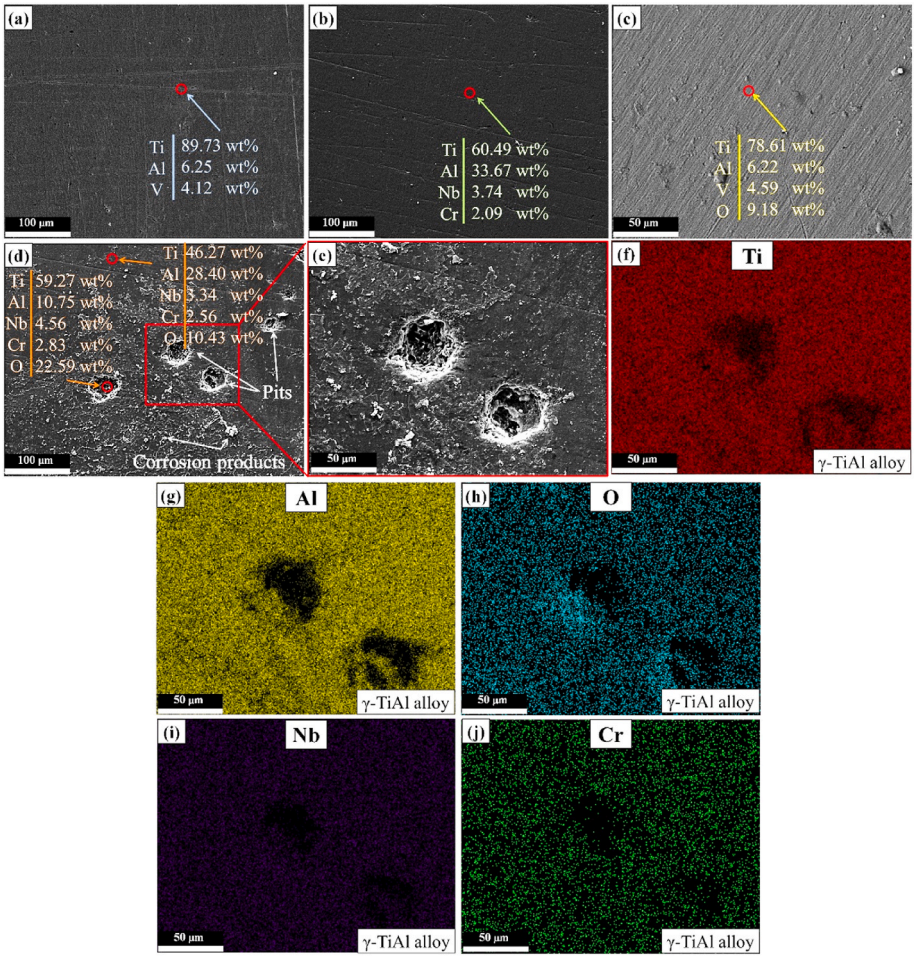

Fig. 6. (a) The SEM of EB-PBF-produced Ti6Al4V and γ-TiAl alloy (a,b) before and (c,d) after potentiodynamic polarisation in 0.9%NaCl solution, (e) high magnification of pit morphologies of γ-TiAl alloy, and (f–j) EDS map analysis.

distribution for Nb and Cr remain relatively unchanged before and after immersion. This confirms that Ti and Al play a significant role in the corrosion and protection of the alloy through selective dissolution in the form of oxide/hydroxide complexes.

According to the literature, the stability, composition, and compactness of a passive film are closely related to its electronic properties [42,53]. Several factors, such as the oxidation potential, the pH, and the chloride ion concentration in the solution, influence these characteristics. When the passive oxide layer is well-formed and compact, it acts as an effective barrier that prevents oxygen atoms from migrating to the metal/oxide interface and participating in further electrochemical reactions. The growth and breakdown of the passive film under steady-state conditions can be explained by the point defect model (PDM), which describes the behaviour of defects at the micro level. This model provides insights into the mechanisms underlying the formation and degradation of passive films [46,54].

Based on the PDM described in Ref. [54], defects in passive films can be classified into different types depending on whether they are associated with n-type or p-type characteristics. In the PDM, oxygen vacancies and cation interstitials are considered as defects associated with n-type behaviour, while cation vacancies impart a p-type character to the passive film. Cation vacancies are consumed at the interface between the metal and the passive layer, while oxygen vacancies are eliminated at the interface between the passive layer and the solution. This results in opposing directions of the fluxes of these point defects.

Previous studies have reported that five main reactions occur during corrosion in an aqueous solution involving the titanium substrate, passive film, and solution [37]. Jiang et al. [51] proposed a cation-anion-vacancy condensation mechanism to explain the pit nucleation process of titanium-based alloys based on the PDM. This mechanism suggests that the presence of chloride ions (Cl^-) in the solution catalyses the generation of cation vacancies within the passive film. The presence of Cl^- ions facilitates the formation of cation vacancies, which are involved in the nucleation of pits on the surface of Ti-based alloys.

In the case of γ-TiAl alloy, it has been observed that aluminium has a higher affinity for oxidation compared to titanium [39]. Previous studies have investigated the effects of Al as an alloying element with lower valencies than titanium on destabilising the surface films formed on Ti-based alloys. It has been suggested that Al^{3+} ions may enter the titanium lattice as interstitial substituents. Consequently, a portion of the aluminium oxide is located on the titanium dioxide layer and penetrates into the TiO_2 matrix. The addition of aluminium to titanium alloys and the subsequent dissolution of aluminium oxide can destabilise the TiO_2 layer in the γ-TiAl alloy [55].

Based on the PDM and present research findings, a schematic model showing the passive film growth process and the mechanism of pitting corrosion on EB-PBF produced γ-TiAl is presented in Fig. 7. The model includes reactions (5–18), that describe the relevant processes involved.

$$Al \rightarrow Al_{Al} + 3/2V_O^{\bullet\bullet} + 3e' \quad (5)$$

$$Ti \rightarrow Ti_{Ti} + 2V_O^{\bullet\bullet} + 4e' \quad (6)$$

$$Ti_{Ti} \rightarrow 2Ti_{Al'} + V_O^{\bullet\bullet} \quad (7)$$

$$Ti + V_{Ti}^{4'} \rightarrow Ti_{Ti} + V_{Ti} + 4e' \quad (8)$$

$$V_O^{\bullet\bullet} + H_2O \rightarrow O_O + 2H^+ \quad (9)$$

$$4V_O^{\bullet\bullet} + 2V_{Ti}^{4'} \leftrightarrow Null' \quad (10)$$

$$3V_O^{\bullet\bullet} + 2V_{Al}^{3'} \leftrightarrow Null' \quad (11)$$

$$Ti_{Al'} \rightarrow Al_{(aq)}^{3+} + V_{Ti}^{4'} \quad (12)$$

$$Al_{Al} \rightarrow Al_{(aq)}^{3+} + V_{Al}^{3'} \quad (13)$$

$$Ti_{Ti} \rightarrow Ti_{(aq)}^{4+} + V_{Ti}^{4'} \quad (14)$$

$$V_O^{\bullet\bullet} + Cl^- \bullet n\,H_2O \rightarrow Cl_O^{\bullet} + nH_2O \quad (15)$$

$$Ti_{Ti} + Cl_O^{\bullet} \leftrightarrow Cl^- \bullet nH2O + \left(V_O^{\bullet\bullet} + V_{Ti}^{4'}\right) + Ti_{(aq)}^{4+} \quad (16)$$

$$Al_{Al} + Cl_O^{\bullet} \leftrightarrow Cl^- \bullet nH2O + \left(V_O^{\bullet\bullet} + V_{Al}^{3'}\right) + Al_{(aq)}^{3+} \quad (17)$$

$$Ti_{Al'} + Cl_O^{\bullet} \leftrightarrow Cl^- \bullet nH2O + \left(V_O^{\bullet\bullet} + V_{Ti}^{4'}\right) + Al_{(aq)}^{3+} \quad (18)$$

The reactions and defects that occur within the passive film, including anionic and cationic vacancies, can be represented using Kröger-Vink notation [37]. In the passive film, Ti and Al, being metal atoms, undergo oxidation and exist as Ti_{Ti}, $Ti_{Al'}$, and Al_{Al}, representing Ti ions in the Ti cation site, Al ions in the Ti cation site, and Al ions in the Al cation site of the passive film, respectively. $V_O^{\bullet\bullet}$, $V_{Ti}^{4'}$ and $V_{Al}^{3'}$ represent oxygen, Ti, and Al ion vacancies within the passive film, while V_{Ti} denotes vacancies in the Ti substrate. *e'* refers to an electron, *Oo* signifies an oxygen ion in the anion site of the passive film, and $Ti_{(aq)}^{4+}$ and $Al_{(aq)}^{3+}$ represent Ti and Al ions in the solution.

In equations (5)–(7), it is mentioned that as corrosion progresses, Ti and Al are oxidised, resulting in the production of oxygen vacancies ($V_O^{\bullet\bullet}$) a means of charge compensation [37]. In addition, Al ions, acting as impurities or dopants, tend to substitute titanium ions in the passive film due to their lower formation energy [39]. This substitution of Al cation in the Ti cation site of $Ti_{Ti,}$ as mentioned in equation (7), generates more oxygen vacancies in the passive film, resulting in a negative charge ($Ti_{Al'}$). It is worth mentioning that this condition is similar to the oxygen vacancy generation by the oxidation of Ti^{3+} and Ti^{2+} to Ti^{4+} due to charge compensation in the passive layer of pure titanium [51,56].

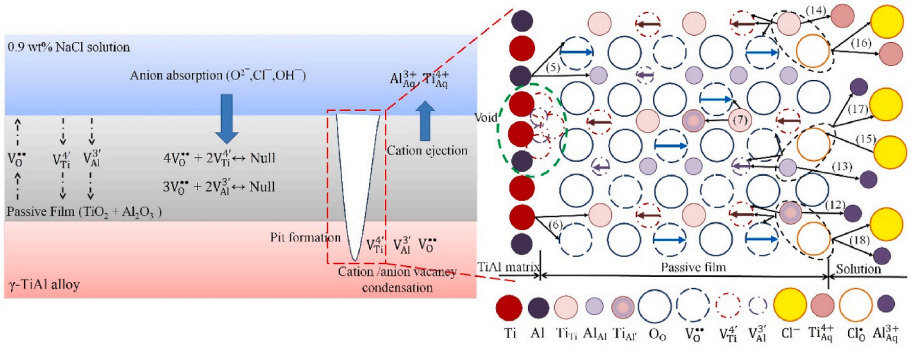

Fig. 7. Schematic diagram of passive film growth and pit formation mechanism based on the point defect model on EB-PBF-produced γ-TiAl in 0.9 % NaCl solution.

Consequently, a significant number of oxygen vacancies $V_O^{\bullet\bullet}$ exist within the passive film. These vacancies then migrate towards the film/solution interface in the direction of the electric field. Simultaneously, according to equation (9), $V_O^{\bullet\bullet}$ reacts with H_2O, leading to the occupation of vacancies by O_2^- ions and the introduction of Oo into the passive film. This reaction between $V_O^{\bullet\bullet}$ and H_2O illustrates the formation and growth of the passive film [57]. However, the consumption of $V_O^{\bullet\bullet}$ due to this reaction creates a charge imbalance, which promotes the Schottky reaction and the formation of $V_{Ti}^{4'}$ and $V_{Al}^{3'}$/ $V_O^{\bullet\bullet}$ pairs (equations (10) and (11)) [37,51].

Once equations (12)–(14) occur, many cation vacancies are generated and diffuse towards the metal/film interface. As a result, Ti and Al atoms occupy these $V_{Ti}^{4'}$ and $V_{Al}^{3'}$ vacancies within the passive film, creating vacancies (V_{Ti}, V_{Al}) in the substrate. This process can be considered as an annihilation reaction (Equation (8)) [51]. However, if there is an excess of unannihilated $V_{Ti}^{4'}$ and $V_{Al}^{3'}$ vacancies that have not been filled in time, they can condense together, forming a void at the metal/film interface (indicated by the green dashed ellipse in Fig. 7). This void disrupts the integrity of the passive film, acting as a starting point for the formation and propagation of pits, marking the onset of pitting corrosion.

The impact of Cl^- on the degradation of the passive layer can be elucidated by considering equations (15)–(18). The elevated electronegativity of Cl^- may lead to its entrapment within the $V_O^{\bullet\bullet}$ structure, leading to the formation of $Cl_O^{\bullet}$ (Equation (15)). This presence of Cl^- in the solution would inhibit the reaction between $V_O^{\bullet\bullet}$ and H_2O, while also affecting the transport of Oo within the passive film. Moreover, $Cl_O^{\bullet}$ interacts with Ti_{Ti}, $Ti_{Al'}$, Al_{Al} within the passive film, facilitating the creation of cation/oxygen vacancies pairs ($V_{Ti}^{4'}$ and $V_{Al}^{3'}$/ $V_O^{\bullet\bullet}$) according to equation 16–18 [37,57]. Subsequent to this, cation vacancies species originating from the solution/film migrate towards the film/alloy boundary and are removed by Ti, as depicted in Equation (8) [58]. Nevertheless, as mentioned before, if an excess of $V_{Ti}^{4'}$ and $V_{Al}^{3'}$ vacancies are not promptly eliminated, they can accumulate at the film/alloy interface, resulting in the formation of voids [57].

In summary, it can be concluded that in γ-TiAl alloys, compared to Ti6Al4V, the incorporation of Al ions into the passive film leads to the formation of more oxygen vacancies within the passive layer (equation (5)). This results in the ejection of metal cations (equations (12) and (13)) at the film/solution interface, generating a greater number of cation vacancies, which then migrate towards the metal/film interface [54]. When more cation vacancies are created, the connections between vacancies become more pronounced, resulting in the formation of voids (known as pit nucleation). Although most voids repassivate immediately upon exposure, a few of them persist and act as nucleation sites for stable pits. The quantity of pits that can survive is directly proportional to the number of voids. When the density of stable pits reaches a critical value, the stability of the oxide layer is significantly reduced. This critical density corresponds to the critical pitting potential. At this potential, the alloy is more prone to the nucleation and growth of stable pits, indicating the onset of pitting corrosion.

4. Conclusions

The aim of this study was to explore the electrochemical behaviour and mechanisms of γ-TiAl produced by the electron beam powder bed fusion process using various electrochemical measurements and microstructural characterisation techniques. The key findings can be summarised as follows:

- The corrosion potential and corrosion current density of the γ-TiAl intermetallic alloy are comparable to those of the Ti6Al4V sample. These results indicate that the γ-TiAl alloy exhibits excellent corrosion resistance when exposed to 0.9 % NaCl solutions.
- The potentiodynamic polarisation curve displayed a consistent passive current density for both samples. However, the presence of higher aluminium content in the γ-TiAl sample caused an increased introduction of Al^{3+} ions into the titanium oxide lattice. This, in turn, contributed to the occurrence of pitting corrosion and the formation of an aluminium depletion zone around the pits.
- The combination of EIS and Motty-Schottky tests suggests that the passive layer formed on γ-TiAl is thicker, has a lower polarisation resistance, and contains more defects with a higher donor density value compared to the passive film on Ti6Al4V. These factors together contribute to affect the corrosion resistance of γ-TiAl.
- The concentration of Al ions released from the γ-TiAl produced by EB-PBF was higher than Ti6Al4V. This was attributed to the higher Al content in the γ-TiAl matrix and the higher oxygen vacancy density of the passive film for the γ-TiAl sample, which increased the dissolution rate.
- According to the point defect model, the presence of higher aluminium content in the γ-TiAl sample leads to an increase in the density of cationic vacancies within the passive films. Consequently, these cationic vacancies tend to aggregate and form voids at the interface between the metal and the film, leading to a localised disruption of the passive film. As a result, pits are initiated at these sites, leading to pitting corrosion.

CRediT authorship contribution statement

Amir behjat: Writing – original draft, Methodology, Investigation, Formal analysis, Data curation. **Abdollah Saboori:** Writing – review & editing, Supervision, Formal analysis, Conceptualization. **Manuela Galati:** Writing – review & editing, Data curation, Conceptualization. **Luca Iuliano:** Writing – review & editing, Resources, Funding acquisition.

Declaration of competing interest

The authors declare that they have no known competing financial interests or personal relationships that could have appeared to influence the work reported in this paper.

Data availability

Data will be made available on request.

References

[1] E. Davoodi, H. Montazerian, A.S. Mirhakimi, M. Zhianmanesh, O. Ibhadode, S. I. Shahabad, R. Esmaeilizadeh, E. Sarikhani, S. Toorandaz, S.A. Sarabi, R. Nasiri, Y. Zhu, J. Kadkhodapour, B. Li, A. Khademhosseini, E. Toyserkani, Additively manufactured metallic biomaterials, Bioact. Mater. 15 (2022) 214–249, https://doi.org/10.1016/j.bioactmat.2021.12.027.
[2] M. Salmi, Additive manufacturing processes in medical applications, Materials 14 (2021) 191, https://doi.org/10.3390/ma14010191.
[3] L.C. Zhang, L.Y. Chen, A review on biomedical titanium alloys: recent progress and prospect, Adv. Eng. Mater. 21 (2019) 1801215, https://doi.org/10.1002/adem.201801215.
[4] Y.W. Cui, L. Wang, L.C. Zhang, Towards load-bearing biomedical titanium-based alloys: from essential requirements to future developments, Prog. Mater. Sci. 144 (2024) 101277, https://doi.org/10.1016/j.pmatsci.2024.101277.
[5] F. Trevisan, F. Calignano, A. Aversa, G. Marchese, M. Lombardi, S. Biamino, D. Ugues, D. Manfredi, Additive manufacturing of titanium alloys in the biomedical field: processes, properties and applications, J. Appl. Biomater. Funct. Mater. 16 (2018) 57–67, https://doi.org/10.5301/jabfm.5000371.
[6] M. Sarraf, E. Rezvani Ghomi, S. Alipour, S. Ramakrishna, N. Liana Sukiman, A state-of-the-art review of the fabrication and characteristics of titanium and its alloys for biomedical applications, Bio-Design Manuf 5 (2022) 371–395, https://doi.org/10.1007/s42242-021-00170-3.
[7] Y. Gu, Y. Sun, S. Shujaat, A. Braem, C. Politis, R. Jacobs, 3D-printed porous Ti6Al4V scaffolds for long bone repair in animal models: a systematic review, J. Orthop. Surg. Res. 17 (2022) 68, https://doi.org/10.1186/s13018-022-02960-6.
[8] A. Behjat, S. Sanaei, M.H. Mosallanejad, M. Atapour, M. Sheikholeslam, A. Saboori, L. Iuliano, A novel titanium alloy for load-bearing biomedical implants: evaluating the antibacterial and biocompatibility of Ti536 produced via electron beam

powder bed fusion additive manufacturing process, Biomater. Adv. 163 (2024) 213928, https://doi.org/10.1016/j.bioadv.2024.213928.
[9] G. Khadija, A. Saleem, Z. Akhtar, Z. Naqvi, M. Gull, M. Masood, S. Mukhtar, M. Batool, N. Saleem, T. Rasheed, N. Nizam, A. Ibrahim, F. Iqbal, Short term exposure to titanium, aluminum and vanadium (Ti 6Al 4V) alloy powder drastically affects behavior and antioxidant metabolites in vital organs of male albino mice, Toxicol Rep 5 (2018) 765–770, https://doi.org/10.1016/j.toxrep.2018.06.006.
[10] J. Tjandra, E. Alabort, D. Barba, S. Pedrazzini, Corrosion, fatigue and wear of additively manufactured Ti alloys for orthopaedic implants, Mater. Sci. Technol. 39 (2023) 2951–2965, https://doi.org/10.1080/02670836.2023.2230417.
[11] M.H. Mosallanejad, A. Abdi, F. Karpasand, N. Nassiri, L. Iuliano, A. Saboori, Additive manufacturing of titanium alloys; processability, properties and applications, Adv. Eng. Mater. 2301122 (2023) 1–29, https://doi.org/10.1002/adem.202301122.
[12] P.A. Sundaram, Cronicon the Potential of Gamma Titanium Aluminides for Implant Applications, 2022.
[13] H.A. Soliman, M. Elbestawi, Titanium aluminides processing by additive manufacturing – a review, Int. J. Adv. Manuf. Technol. 119 (2022) 5583–5614, https://doi.org/10.1007/s00170-022-08728-w.
[14] A. Emiralioğlu, R. Ünal, Additive manufacturing of gamma titanium aluminide alloys: a review, J. Mater. Sci. 57 (2022) 4441–4466, https://doi.org/10.1007/s10853-022-06896-4.
[15] B. Jin, Q. Wang, L. Zhao, A. Pan, X. Ding, W. Gao, Y. Song, X. Zhang, A review of additive manufacturing techniques and post-processing for high-temperature titanium alloys, Metals 13 (2023) 1327, https://doi.org/10.3390/met13081327.
[16] W. Chen, Z. Li, Additive Manufacturing of Titanium Aluminides, Elsevier Inc., 2019, pp. 235–263, https://doi.org/10.1016/B978-0-12-814062-8.00013-3.
[17] L.Y. Chen, S.X. Liang, Y. Liu, L.C. Zhang, Additive manufacturing of metallic lattice structures: unconstrained design, accurate fabrication, fascinated performances, and challenges, Mater. Sci. Eng. R Rep. 146 (2021) 100648, https://doi.org/10.1016/j.mser.2021.100648.
[18] L.Y. Chen, P. Qin, L. Zhang, L.C. Zhang, An overview of additively manufactured metal matrix composites: preparation, performance, and challenge, Int. J. Extrem. Manuf. 6 (2024) 052006, https://doi.org/10.1088/2631-7990/ad54a4.
[19] L.E. Murr, S.M. Gaytan, D.A. Ramirez, E. Martinez, J. Hernandez, K.N. Amato, P. W. Shindo, F.R. Medina, R.B. Wicker, Metal fabrication by additive manufacturing using laser and electron beam melting technologies, J. Mater. Sci. Technol. 28 (2012) 1–14, https://doi.org/10.1016/S1005-0302(12)60016-4.
[20] R. Wartbichler, H. Clemens, S. Mayer, C. Ghibaudo, G. Rizza, M. Galati, L. Iuliano, S. Biamino, D. Ugues, On the formation mechanism of banded microstructures in electron beam melted Ti–48Al–2Cr–2Nb and the design of heat treatments as remedial action, Adv. Eng. Mater. 23 (2021) 2101199, https://doi.org/10.1002/adem.202101199.
[21] L.E. Murr, S.M. Gaytan, A. Ceylan, E. Martinez, J.L. Martinez, D.H. Hernandez, B. I. Machado, D.A. Ramirez, F. Medina, S. Collins, R.B. Wicker, Characterization of titanium aluminide alloy components fabricated by additive manufacturing using electron beam melting, Acta Mater. 58 (2010) 1887–1894, https://doi.org/10.1016/j.actamat.2009.11.032.
[22] S. Biamino, A. Penna, U. Ackelid, S. Sabbadini, O. Tassa, P. Fino, M. Pavese, P. Gennaro, C. Badini, Electron beam melting of Ti-48Al-2Cr-2Nb alloy: microstructure and mechanical properties investigation, Intermetallics 19 (2011) 776–781, https://doi.org/10.1016/j.intermet.2010.11.017.
[23] A. Takase, Residual stress and phase stability of titanium alloys fabricated by laser and electron beam powder bed fusion Techniques+1, Mater. Trans. 64 (2023) 17–24, https://doi.org/10.2320/matertrans.MT-MLA2022004.
[24] D. Wimler, J. Lindemann, M. Reith, A. Kirchner, M. Allen, W.G. Vargas, M. Franke, B. Klöden, T. Weißgärber, V. Güther, M. Schloffer, H. Clemens, S. Mayer, Designing advanced intermetallic titanium aluminide alloys for additive manufacturing, Intermetallics 131 (2021) 107109, https://doi.org/10.1016/j.intermet.2021.107109.
[25] J. Moritz, M. Teschke, A. Marquardt, L. Stepien, E. López, F. Brückner, M. Macias Barrientos, F. Walther, C. Leyens, Electron beam powder bed fusion of γ-titanium aluminide: effect of processing parameters on part density, surface characteristics and aluminum content, Metals 11 (2021) 71093, https://doi.org/10.3390/met11071093.
[26] P.L. Narayana, J.H. Kim, D.W. Yun, S.E. Kim, N.S. Reddy, J.T. Yeom, D. Seo, J. K. Hong, High temperature isothermal oxidation behavior of electron beam melted multi-phase γ-TiAl alloy, Intermetallics 141 (2022) 107424, https://doi.org/10.1016/j.intermet.2021.107424.
[27] Y.K. Kim, S.J. Youn, S.W. Kim, J. Hong, K.A. Lee, High-temperature creep behavior of gamma Ti-48Al-2Cr-2Nb alloy additively manufactured by electron beam melting, Mater. Sci. Eng. 763 (2019) 138138, https://doi.org/10.1016/j.msea.2019.138138.
[28] H.S. Abdo, U.A. Samad, J.A. Mohammed, S.A. Ragab, A.H. Seikh, Mitigating corrosion effects of Ti-48Al-2Cr-2Nb alloy fabricated via electron beam melting (EBM) technique by regulating the immersion conditions. https://doi.org/10.3390/cryst11080889, 2021.
[29] A. Mohammad, A.M. Al-Ahmari, V.K. Balla, M. Das, S. Datta, D. Yadav, G.D. Janaki Ram, In vitro wear, corrosion and biocompatibility of electron beam melted γ-TiAl, Mater. Des. 133 (2017) 186–194, https://doi.org/10.1016/j.matdes.2017.07.065.
[30] M. Galati, G. Rizza, S. Defanti, L. Denti, Surface roughness prediction model for Electron Beam Melting (EBM) processing Ti6Al4V, Precis. Eng. 69 (2021) 19–28, https://doi.org/10.1016/j.precisioneng.2021.01.002.
[31] G. Del Guercio, M. Galati, A. Saboori, P. Fino, L. Iuliano, Microstructure and mechanical performance of Ti–6Al–4V lattice structures manufactured via electron beam melting (ebm): a review, Acta Metall. Sin. (English Lett. 33 (2020) 183–203, https://doi.org/10.1007/s40195-020-00998-1.
[32] G. Del Guercio, M. Galati, A. Saboori, Innovative approach to evaluate the mechanical performance of Ti–6Al–4V lattice structures produced by electron beam melting process, Met. Mater. Int. 27 (2021) 55–67, https://doi.org/10.1007/s12540-020-00745-2.
[33] M. Todai, T. Nakano, T. Liu, H.Y. Yasuda, K. Hagihara, K. Cho, M. Ueda, M. Takeyama, Effect of building direction on the microstructure and tensile properties of Ti-48Al-2Cr-2Nb alloy additively manufactured by electron beam melting, Addit. Manuf. 13 (2017) 61–70, https://doi.org/10.1016/j.addma.2016.11.001.
[34] T.C. Dzogbewu, Additive manufacturing of TiAl-based alloys, Manuf. Rev. 7 (2020) 35, https://doi.org/10.1051/mfreview/2020032.
[35] Y. Chen, H. Yue, X. Wang, S. Xiao, F. Kong, X. Cheng, H. Peng, Selective electron beam melting of TiAl alloy: microstructure evolution, phase transformation and microhardness, Mater. Char. 142 (2018) 584–592, https://doi.org/10.1016/j.matchar.2018.06.027.
[36] V. Dehnavi, J.D. Henderson, C. Dharmendra, B.S. Amirkhiz, D.W. Shoesmith, J. J. Noël, M. Mohammadi, Corrosion behaviour of electron beam melted Ti6Al4V: effects of microstructural variation, J. Electrochem. Soc. 167 (2020) 131505, https://doi.org/10.1149/1945-7111/abb9d1.
[37] Y.W. Cui, L.Y. Chen, Y.H. Chu, L. Zhang, R. Li, S. Lu, L. Wang, L.C. Zhang, Metastable pitting corrosion behavior and characteristics of passive film of laser powder bed fusion produced Ti–6Al–4V in NaCl solutions with different concentrations, Corrosion Sci. 215 (2023) 111017, https://doi.org/10.1016/j.corsci.2023.111017.
[38] Y.W. Cui, L.Y. Chen, P. Qin, R. Li, Q. Zang, J. Peng, L. Zhang, S. Lu, L. Wang, L. C. Zhang, Metastable pitting corrosion behavior of laser powder bed fusion produced Ti-6Al-4V in Hank's solution, Corrosion Sci. 203 (2022) 110333, https://doi.org/10.1016/j.corsci.2022.110333.
[39] H.M. Saffarian, Q. Gan, R. Hadkar, G.W. Warren, Corrosion behavior of binary titanium aluminide intermetallics, Mater. Org. (Berl.) 52 (1996) 626–633, https://doi.org/10.5006/1.3292153.
[40] H. Li, Y. Zheng, J. Lin, Comparative evaluation on the in vitro biological performance of Ti45Al8.5Nb intermetallic with Ti6Al4V and Ti6Al7Nb Alloys, Adv. Eng. Mater. 13 (2011) 80110, https://doi.org/10.1002/adem.201080110.
[41] Y. Wang, Z. Xu, T. Geng, Y. Teng, Electrochemical dissolution behavior of TNM intermetallic in sodium nitrate solution, J. Mater. Res. Technol. 25 (2023) 5950–5963, https://doi.org/10.1016/j.jmrt.2023.07.031.
[42] X. Gai, Y. Bai, J. Li, S. Li, W. Hou, Y. Hao, X. Zhang, R. Yang, R.D.K. Misra, Electrochemical behaviour of passive film formed on the surface of Ti-6Al-4V alloys fabricated by electron beam melting, Corrosion Sci. 145 (2018) 80–89, https://doi.org/10.1016/j.corsci.2018.09.010.
[43] A. Behjat, M. Shamanian, A. Taherizadeh, E. Lannunziata, S. Bagherifard, E. Gadalińska, A. Saboori, L. Iuliano, Microstructure-electrochemical behavior relationship in post processed AISI316L stainless steel parts fabricated by laser powder bed fusion, J. Mater. Res. Technol. 23 (2023) 3294–3311, https://doi.org/10.1016/j.jmrt.2023.01.229.
[44] G.J. Brug, A.L.G. van den Eeden, M. Sluyters-Rehbach, J.H. Sluyters, The analysis of electrode impedances complicated by the presence of a constant phase element, J. Electroanal. Chem. Interfacial Electrochem. 176 (1984) 275–295, https://doi.org/10.1016/S0022-0728(84)80324-1.
[45] R. Swadźba, K. Marugi, Pyclik, STEM investigations of γ-TiAl produced by additive manufacturing after isothermal oxidation, Corrosion Sci. 169 (2020) 108617, https://doi.org/10.1016/j.corsci.2020.108617.
[46] A. Fattah-alhosseini, F. Soltani, F. Shirsalimi, B. Ezadi, N. Attarzadeh, The semiconducting properties of passive films formed on AISI 316 L and AISI 321 stainless steels: a test of the point defect model (PDM), Corrosion Sci. 53 (2011) 3186–3192, https://doi.org/10.1016/j.corsci.2011.05.063.
[47] J. Guo, H. Yu, H. Meng, D. Sun, Correlation between corrosion behaviour and semiconductor characteristics of passive film on incoloy 825 in ammonium chloride solution, Int. J. Electrochem. Sci. 15 (2020) 4264–4273, https://doi.org/10.20964/2020.05.10.
[48] G. Sander, A.P. Babu, X. Gao, D. Jiang, N. Birbilis, On the effect of build orientation and residual stress on the corrosion of 316L stainless steel prepared by selective laser melting, Corrosion Sci. 179 (2021) 109149, https://doi.org/10.1016/j.corsci.2020.109149.
[49] S. Memarbashi, E. Saebnoori, T. Shahrabi, A study on the passivation behavior and semiconducting properties of gamma titanium aluminide in 0.1 N H2SO4, HNO3, and HClO4 acidic solutions, J. Mater. Eng. Perform. 23 (2014) 912–917, https://doi.org/10.1007/s11665-013-0840-4.
[50] D.-I. Seo, J.-B. Lee, Localized corrosion and repassivation behaviors of additively manufactured titanium alloys in simulated biomedical solutions, npj Mater. Degrad. 7 (2023) 44, https://doi.org/10.1038/s41529-023-00363-4.
[51] Z. Jiang, X. Dai, T. Norby, H. Middleton, Investigation of pitting resistance of titanium based on a modified point defect model, Corrosion Sci. 53 (2011) 815–821, https://doi.org/10.1016/j.corsci.2010.11.015.
[52] Y. Shi, B. Yang, X. Xie, J. Brechtl, K.A. Dahmen, P.K. Liaw, Corrosion of Al xCoCrFeNi high-entropy alloys: Al-content and potential scan-rate dependent pitting behavior, Corrosion Sci. 119 (2017) 33–45, https://doi.org/10.1016/j.corsci.2017.02.019.
[53] D.D. Macdonald, The point defect model for the passive state, J. Electrochem. Soc. 139 (1992) 3434–3449, https://doi.org/10.1149/1.2069096.
[54] D.D. Macdonald, The history of the Point Defect Model for the passive state: a brief review of film growth aspects, Electrochim. Acta 56 (2011) 1761–1772, https://doi.org/10.1016/j.electacta.2010.11.005.

[55] M. Ruzickova, H. Hildebrand, S. Virtanen, On the stability of passivity of Ti-Al alloys in acidic environment, Zeitschrift Fur Phys. Chemie. 219 (2005) 1447–1459, https://doi.org/10.1524/zpch.2005.219.11.1447.
[56] M. Metikoš-Huković, A. Kwokal, J. Piljac, The influence of niobium and vanadium on passivity of titanium-based implants in physiological solution, Biomaterials 24 (2003) 3765–3775, https://doi.org/10.1016/S0142-9612(03)00252-7.
[57] T. Qin, X. Lin, J. Yu, M. Wang, P. Guo, J. Li, Y. Zhang, J. Liu, S. Zhang, W. Huang, Performance of different microstructure on electrochemical behaviors of laser solid formed Ti–6Al–4V alloy in NaCl solution, Corrosion Sci. 185 (2021) 109392, https://doi.org/10.1016/j.corsci.2021.109392.
[58] H. Liu, H. Liu, S. Zhang, H. Wang, X. Wei, L. Ren, K. Yang, Metastable pitting corrosion behavior of laser powder bed fusion produced Ti6Al4V-Cu in 3.5% NaCl solution, Corrosion Sci. 223 (2023) 111452, https://doi.org/10.1016/j.corsci.2023.111452.